

Direction-dependent optical modes in nanoscale Silicon waveguides

Jacob T. Robinson^{1,3} and Michal Lipson^{1,2,*}

¹School of Electrical and Computer Engineering, Cornell University, Ithaca, NY 14853 USA

²Kavli Institute at Cornell for Nanoscale Science, Cornell University, Ithaca, NY 14853 USA

³Current address: Department of Chemistry and Chemical Biology, Harvard University, Cambridge, MA 02138 USA
[*ml292@cornell.edu](mailto:ml292@cornell.edu)

Abstract: We show that in high-index-contrast nanoscale waveguides counter propagating waves can possess distinct spatial near-field profiles. Using transmission-based near-field scanning optical microscopy (TraNSOM), we identify and map the unique near-field intensity distributions of these counter-propagating modes in a single-mode silicon waveguide. Based on this phenomenon, we design and simulate an integrated device 45 μm in length that selectively attenuates reflected light with an insertion loss of -3.6 dB and an extinction of greater than -20 dB.

©2011 Optical Society of America

OCIS codes: (130.2790) Guided waves; (230.3204) Isolators; (180.4243) Near-field microscopy.

References and links

1. H. Cho, P. K'apur, and K. C. Saraswat, "Power Comparison Between High-Speed Electrical and Optical Interconnects for Interchip Communication," *J. Lightwave Technol.* **22**(9), 2021–2033 (2004).
2. M. Lipson, "Guiding, modulating, and emitting light on Silicon-challenges and opportunities," *J. Lightwave Technol.* **23**(12), 4222–4238 (2005).
3. R. Soref, "The Past, Present, and Future of Silicon Photonics," *IEEE J. Sel. Top. Quant.* **12**(6), 1678–1687 (2006).
4. T. Barwicz, H. Byun, F. Gan, C. W. Holzwarth, M. A. Popovic, P. T. Rakich, M. R. Watts, E. P. Ippen, F. X. Kärtner, H. I. Smith, J. S. Orcutt, R. J. Ram, V. Stojanovic, O. O. Olubuyide, J. L. Hoyt, S. Spector, M. Geis, M. Grein, T. Lyszczarz, and J. U. Yoon, "Silicon photonics for compact, energy-efficient interconnects," *J. Opt. Net.* **6**(1), 63–73 (2007).
5. A. Liu, R. Jones, L. Liao, D. Samara-Rubio, D. Rubin, O. Cohen, R. Nicolaescu, and M. Paniccia, "A high-speed silicon optical modulator based on a metal-oxide-semiconductor capacitor," *Nature* **427**(6975), 615–618 (2004).
6. V. R. Almeida, C. A. Barrios, R. R. Panepucci, and M. Lipson, "All-optical control of light on a silicon chip," *Nature* **431**(7012), 1081–1084 (2004).
7. Q. Xu, B. Schmidt, S. Pradhan, and M. Lipson, "Micrometre-scale silicon electro-optic modulator," *Nature* **435**(7040), 325–327 (2005).
8. F. Xia, L. Sekaric, and Y. Vlasov, "Ultracompact optical buffers on a silicon chip," *Nat. Photonics* **1**(1), 65–71 (2007).
9. Y. A. Vlasov, M. O'Boyle, H. F. Hamann, and S. J. McNab, "Active control of slow light on a chip with photonic crystal waveguides," *Nature* **438**(7064), 65–69 (2005).
10. S. F. Preble, Q. Xu, and M. Lipson, "Changing the colour of light in a silicon resonator," *Nat. Photonics* **1**(5), 293–296 (2007).
11. M. A. Foster, A. C. Turner, J. E. Sharping, B. S. Schmidt, M. Lipson, and A. L. Gaeta, "Broad-band optical parametric gain on a silicon photonic chip," *Nature* **441**(7096), 960–963 (2006).
12. R. Espinola, J. Dadap, R. Osgood, Jr., S. McNab, and Y. Vlasov, "C-band wavelength conversion in silicon photonic wire waveguides," *Opt. Express* **13**(11), 4341–4349 (2005), <http://www.opticsexpress.org/abstract.cfm?URI=oe-13-11-4341>.
13. M. Borselli, T. Johnson, and O. Painter, "Beyond the Rayleigh scattering limit in high-Q silicon microdisks: theory and experiment," *Opt. Express* **13**(5), 1515–1530 (2005), <http://www.opticsexpress.org/abstract.cfm?URI=oe-13-5-1515>.
14. B. E. A. Saleh and M. C. Teich, *Fundamentals of Photonics* (Wiley-Interscience, 1991)
15. R. Ramaswami and K. N. Sivarajan, *Optical networks: a practical perspective* (Morgan Kaufmann, 2002)
16. R. B. Dyott, *Elliptical Fiber Waveguides* (Artech House Publishers, 1995)
17. L. B. Soldano and E. C. M. Pennings, "Optical multi-mode interference devices based on self-imaging: principles and applications," *J. Lightwave Technol.* **13**(4), 615–627 (1995).

18. S.-H. Kim, R. Takei, Y. Shoji, and T. Mizumoto, "Single-trench waveguide TE-TM mode converter," *Opt. Express* **17**(14), 11267–11273 (2009), <http://www.opticsexpress.org/abstract.cfm?URI=oe-17-14-11267>.
19. Z. Wang and D. Dai, "Ultrasmall Si-nanowire-based polarization rotator," *J. Opt. Soc. Am. B* **25**(5), 747–753 (2008).
20. W. C. L. Hopman, K. O. van der Werf, A. J. F. Hollink, W. Bogaerts, V. Subramaniam, and R. M. de Ridder, "Nano-mechanical tuning and imaging of a photonic crystal micro-cavity resonance," *Opt. Express* **14**(19), 8745–8752 (2006), <http://www.opticsexpress.org/abstract.cfm?URI=oe-14-19-8745>.
21. J. T. Robinson, S. F. Preble, and M. Lipson, "Imaging highly confined modes in sub-micron scale silicon waveguides using Transmission-based Near-field Scanning Optical Microscopy," *Opt. Express* **14**(22), 10588–10595 (2006), <http://www.opticsexpress.org/abstract.cfm?URI=oe-14-22-10588>.
22. M. Abashin, U. Levy, K. Ikeda, and Y. Fainman, "Effects produced by metal-coated near-field probes on the performance of silicon waveguides and resonators," *Opt. Lett.* **32**(17), 2602–2604 (2007), <http://ol.osa.org/abstract.cfm?URI=ol-32-17-2602>.
23. B. Cluzell, L. Lalouat, P. Velha, E. Picard, D. Peyrade, J.-C. Rodier, T. Charvolin, P. Lalanne, F. de Fornel, and E. Hadji, "A near-field actuated optical nanocavity," *Opt. Express* **16**(1), 279–286 (2008), <http://www.opticsexpress.org/abstract.cfm?URI=oe-16-1-279>.
24. L. Lalouat, B. Cluzel, F. de Fornel, P. Velha, P. Lalanne, D. Peyrade, E. Picard, T. Charvolin, and E. Hadji, "Subwavelength imaging of light confinement in high-Q/small-V photonic crystal nanocavity," *Appl. Phys. Lett.* **92**(11), 111111 (2008).
25. M. Abashin, P. Tortora, I. Märki, U. Levy, W. Nakagawa, L. Vaccaro, H. Herzig, and Y. Fainman, "Near-field characterization of propagating optical modes in photonic crystal waveguides," *Opt. Express* **14**(4), 1643–1657 (2006), <http://www.opticsexpress.org/abstract.cfm?URI=oe-14-4-1643>.
26. I. Stefanon, S. Blaize, A. Bruyant, S. Aubert, G. Lerondel, R. Bachelot, and P. Royer, "Heterodyne detection of guided waves using a scattering-type Scanning Near-Field Optical Microscope," *Opt. Express* **13**(14), 5553–5564 (2005), <http://www.opticsexpress.org/abstract.cfm?URI=oe-13-14-5553>.
27. M. L. M. Balistreri, H. Gersen, J. P. Korterik, L. Kuipers, and N. F. van Hulst, "Tracking femtosecond laser pulses in space and time," *Science* **294**(5544), 1080–1082 (2001).
28. J. T. Robinson and M. Lipson, "Far-field control of radiation from an individual optical nanocavity: analogue to an optical dipole," *Phys. Rev. Lett.* **100**(4), 043902–043904 (2008).
29. D. Marcuse, *Theory of dielectric optical waveguides* (Academic Press, Inc., 1974), pp. 102–103; 4–5
30. V. R. Almeida, R. R. Panepucci, and M. Lipson, "Nanotaper for compact mode conversion," *Opt. Lett.* **28**(15), 1302–1304 (2003), <http://ol.osa.org/abstract.cfm?URI=ol-28-15-1302>.
31. C. Pollock and M. Lipson, *Integrated Photonics* (Springer, 2003)
32. Y. Vlasov and S. McNab, "Losses in single-mode silicon-on-insulator strip waveguides and bends," *Opt. Express* **12**(8), 1622–1631 (2004), <http://www.opticsexpress.org/abstract.cfm?URI=oe-12-8-1622>.
33. R. Soref and B. Bennett, "Electrooptical effects in silicon," *IEEE J. Quantum Electron.* **23**(1), 123–129 (1987).
34. H. Shimizu and Y. Nakano, "Fabrication and Characterization of an InGaAsP/InP Active Waveguide Optical Isolator With 14.7 dB/mm TE Mode Nonreciprocal Attenuation," *J. Lightwave Technol.* **24**(1), 38–43 (2006).
35. Y. Shoji, T. Mizumoto, H. Yokoi, I. W. Hsieh, and R. M. Osgood, "Magneto-optical isolator with silicon waveguides fabricated by direct bonding," *Appl. Phys. Lett.* **92**(7), 071117–071117 (2008).

1. Introduction

On-chip photonic networks have the potential to transmit and route information more efficiently than electronic circuits [1–4] and recently, a number of silicon-based optical devices have been reported including modulators [5–7], buffers [8, 9], and wavelength converters [10–12]. However, a number of technical challenges need to be overcome before these devices can be combined into network-level architectures. In particular, the high refractive index contrast between the core and cladding, combined with nanoscale defects along the waveguide often cause light to scatter into the backward-propagating mode [13]. These reflections could result in unwanted feedback to optical sources [14] or crosstalk in bi-directional interconnects such as those employed in fiber-optic networks [15]. Understanding the behavior of forward-propagating and reflected modes is particularly important for developing strategies to overcome these potential pitfalls. We report here that nanoscale light confinement and high-index contrast in nanophotonic waveguides can impose unique near-field profiles for counter-propagating waves. These modal differences are not expected for optical propagation in fiber-optic waveguides and represent a unique phenomenon in high-index contrast nanophotonics.

In traditional waveguides, like fiber optics with micron-sized cross sections, forward-propagating and reflected waves spatially overlap. By design, the dimensions of these waveguides allow only one mode to propagate for each orthogonal polarization [14]. Since

the fibers are often radially symmetric (and the difference in refractive index is not large enough to cause significant electric field discontinuities) the orthogonally polarized modes are typically degenerate and their intensity profiles are nearly identical. Propagating light is therefore confined to this single mode and the distribution of optical intensity for forward-propagating and reflected light is identical in the near-field. Even when the degeneracy between orthogonally polarized modes is broken (by introducing asymmetry in the fiber cross-section [16]), reflected light typically remains in the polarization state of the forward-propagating mode, and is therefore indistinguishable based on its near-field intensity distribution. This spatial indistinguishability creates difficulty in separating forward-propagating from reflected light.

Here, using near-field microscopy, we show for the first time that in nanophotonic waveguides, forward-propagating and reflected waves can be spatially distinct and selectively attenuated. We also show that this phenomenon could lead to a new class of integrated anti-reflection devices. We show here that since TE and TM modes in these high-index contrast waveguides are not entirely orthogonally polarized, optical propagation can exhibit beating between these modes. While mode beating between fundamental and higher order modes has been observed and used for a number of devices [17], we show for the first time that this mode beating can occur between modes that are often considered orthogonally polarized. This enables polarization rotators [18, 19] to be used both to select the exact ratio of excitation of the two modes, and convert light back into a pure TE or TM state for use with polarization sensitive components. Furthermore, unlike higher-order mode beating, we show that the interference between TE and TM modes can occur between degenerate modes resulting phase-dependent mode profiles with no beating pattern.

2. Near field measurement of counter-propagating modes

Figure 1 shows a schematic of the experiment by which forward-propagating and reflected light can be identified in the near field. Optical fibers are used to couple light into and out of the silicon waveguide (shown in green). Details of the experimental setup and device fabrication can be found in the Section 6. While scanning the waveguide with an Atomic Force Microscope (AFM) probe we monitor the power transmitted through the device. This technique, Transmission-based Near-field Scanning Optical Microscopy (TraNSOM), was recently developed for imaging near field profiles in high index-contrast-waveguides [20, 21] and subsequently applied to optical resonant cavities [22–24]. Compared to phase-sensitive [25, 26] and time-resolved [27] near-field microscopy techniques which can determine the direction of optical propagation based on the sign of the propagation constant, here we use TraNSOM to search for spatial differences in intensity profiles between forward-propagating and reflected modes. When the probe interacts with the evanescent field of the guided wave it scatters some of the light out of this mode. Since the probe is in the near field of the waveguide, much of this scattered light couples back into the guided mode and propagates in a direction opposite to the incident light [13]. This is measured as a probe-induced reflection and can be used to determine the propagation direction of the incident light. For instance, when the probe interacts with the forward-propagating mode, light is reflected away from the output and the transmitted power decreases. Conversely, when the probe interacts with the backward-propagating reflected light, probe-induced reflection redirects some of this light toward the output. Thus probe interaction with the reflected light results in an increase in the optical power detected at the output. By monitoring the transmission changes of opposite sign, we aim to distinguish forward-propagating from reflected light. If the mode profiles of the forward-propagating and reflected waves are identical (as is expected for low-index waveguides like fiber optics) we should observe that scattering by the probe only decreases the transmitted power. This is because at every point across the waveguide, the probe would interact simultaneously with both forward-propagating and reflected light. Due to propagation losses, the amplitude of the forward propagating mode is larger and would therefore dominate

the measured signal. If, however, the forward-propagating and reflected waves are spatially separated (i.e. at specific points across the waveguide the probe interacts with one wave and not the other), we should be able to observe both a decrease and increase in transmission as the probe interacts individually with either the forward-propagating or reflected waves respectively. As will be shown in the subsequent sections, this spatial diversity can arise from reflections induced by waveguide inhomogeneities.

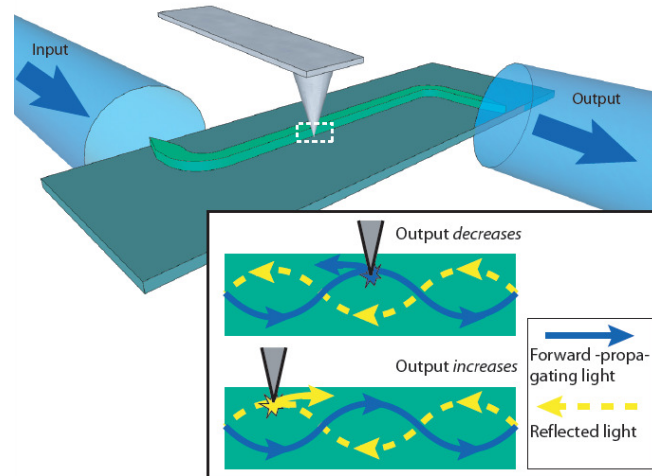


Fig. 1. Schematic of TraNSOM measurement of counter-propagating mode profiles. Fiber optics couple light into and out of the waveguide. The power transmitted through the device is constantly monitored as the waveguide is scanned by an AFM probe. Probe-induced scattering of the forward-propagating or reflected light decrease or increase the output power respectively (inset: solid and dashed lines respectively). Based on the sign of the change in transmitted power, forward-propagating and backward-propagating reflected light can be distinguished.

Figure 2a shows the result of this measurement where both forward-propagating and reflected waves are distinct and clearly visible. The measured topography of the waveguide is shown in the Fig. 2a inset, along with the simultaneously measured transmitted power (Fig. 2a). The measurement is performed with a source wavelength of $1.532\ \mu\text{m}$ (see Section 6). Dark blue regions (point A) indicate a probe-induced *decrease* in transmitted power resulting from interaction with forward-propagating light. Red regions (point B) indicate a probe-induced *increase* in transmitted power resulting from interaction with backward-propagating reflected light. Thus the sign of the transmission change indicates the direction of light propagation. (Note the small changes in transmission when the probe is far from the waveguide are the result of far-field suppression and enhancement of radiation scattered from defects along the waveguide [28]).

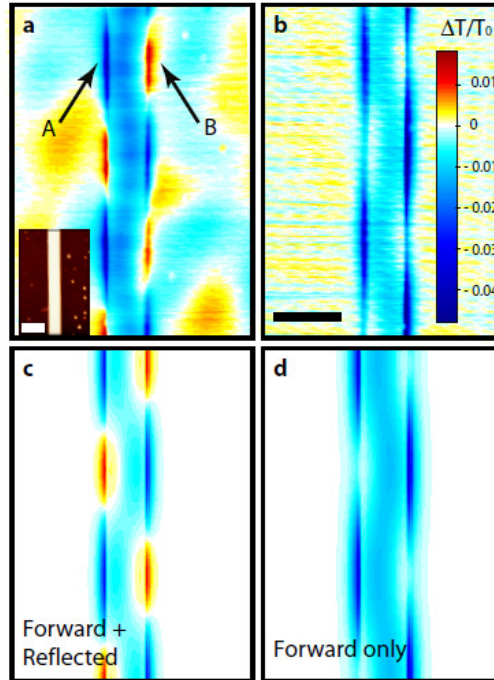


Fig. 2. Measurement and theory of counter-propagating waveguide modes. (a) measured change in transmission as a function of probe position for a 5 μm length of SOI waveguide. Point (A) corresponds to a region where the transmission *decreases* indicating light here is traveling in the *forward* direction. Point (B) corresponds to a region where the transmission *increases* indicating light here is traveling in the *backward* direction. (a inset, bottom left), simultaneously measured AFM topography. (b) change in transmission vs. probe position for the same length of waveguide using a short-coherence-length source which isolates the contribution of forward-propagating mode. The color scale for the relative change in transmission (see b) is the same for (a)-(d). (c), calculated near-field image of the probe-induced change in transmission over a 5 μm segment of waveguide according to our model including both forward-propagating and reflected light. This corresponds to the measured data in (a). (d) calculated near-field image considering only forward propagating light corresponding to (b). Scale bars are 1 μm .

We verify that backward propagating light is responsible for the measured increase in transmission by eliminating its contribution to the measured signal and repeating the TraNSOM measurement. This is achieved using an optical source with a short coherence length. Figure 2b shows the TraNSOM image using an optical source with a 1.4 mm coherence length. Because this coherence length is shorter than the path from the probe to the end of the waveguide and back, by the time the reflected light is scattered by the probe it has no well-defined phase relationship with the forward-propagating light. Therefore the scattered light from the backward-propagating reflected wave is equally likely to constructively or destructively interfere with the forward-propagating mode and thus has no net effect on the transmitted power. Therefore, by using a short-coherence-length source we can selectively map the distribution of only the forward-propagating light. As expected, Fig. 2b shows no probe-induced increases in transmission. This verifies that the measured increase in transmission is the result of interaction with the backward-propagating reflected light in the guided mode. Figure 2c shows a theoretical TraNSOM signal calculated with contributions from both forward-propagating and reflected light. Figure 2d shows the same calculation considering only forward-propagating light. This corresponds to the measured data in Fig. 2a and b respectively. Details of the calculation are described in subsequent sections.

3. Numerical simulations of counter propagating modes

The spatially-distinct near-field profiles observed in Fig. 2 are the result of large minor field components in nanoscale high-index-contrast waveguides. Figure 3a and b show the calculated vertical (y) component of the electric field for the fundamental TM and TE modes respectively. We see in Fig. 3b that although the TE mode is polarized primarily in the horizontal (x) direction there are large minor field components in the y -direction at the waveguide corners. Due to these large minor field components, these modes are frequently referred to as quasi-TE or quasi-TM. This property of large minor field components at the waveguide corners is unique to high-index nanoscale waveguides. In fiber optic waveguides, the index contrast is too small to produce these field components, and thus the shape of the mode profile does not depend on the phase between the TE and TM modes. Note that with regard to the near-field measurements will consider only the y -component of the electric field. This is because the high-aspect-ratio metallic probe used to for TraNSOM measurements predominantly scatters light polarized along the probe axis [21]. A similar analysis would hold for the field polarized in the x -direction, however this polarization component is not measured using our experimental apparatus.

If both TE and TM modes are excited, the total shape of the mode profile is the coherent sum of these two modes. This causes the overall mode profile to “lean” to the left or right depending on the phase difference between the TM and TE modes (see Fig. 3c and d). The degree to which the mode “leans” depends on the relative amplitude of the TE and TM components. Typically, when the forward propagating wave encounters a waveguide perturbation (such as a change in dimensions, neighboring resonant cavity, scattering defect, or cleaved facet), the TE and TM modes will experience different reflection coefficients. These coefficients (which can typically be calculated using coupled mode theory [29]) will result in a backward traveling wave with a new amplitude and phase relationship between the TE and TM modes. Therefore the backward traveling wave will follow a different pattern of propagation relative to the forward traveling wave. For instance, the amplitude and positions of the “leaning” mode will be altered by the new amplitude and phase relationship between the reflected TE and TM components. As we will show in Section 5, the spatial differences between the forward and backward traveling waves, due to reflection by waveguide perturbations, can be utilized to attenuate backward propagating light.

To illustrate the spatial differences between forward and backward propagating modes we consider a π phase shift for the reflected TM mode relative to the TE mode. We expect this relative phase difference from reflection by the inverse taper couplers at the waveguide-fiber interfaces [30] (see Figs. 1 and 4). Since the TM mode ($n_{\text{eff}} = 2.02$) is delocalized compared to the TE mode ($n_{\text{eff}} = 2.48$), its reflection is dominated by the change in cladding from air to photoresist at the coupling regions (see Fig. 4). The resulting increase in refractive index results in a π phase shift according to the Fresnel equations [29]. The more highly confined TE mode however is less sensitive to the change in cladding and is more strongly affected by the change in waveguide width. This results in reflection at a transition to a lower refractive index and therefore the reflected wave experiences a phase shift near zero [29]. The shift in the relative phases of the TE and TM modes causes the backward-propagating wave to “lean” in the opposite direction as the forward-propagating light.

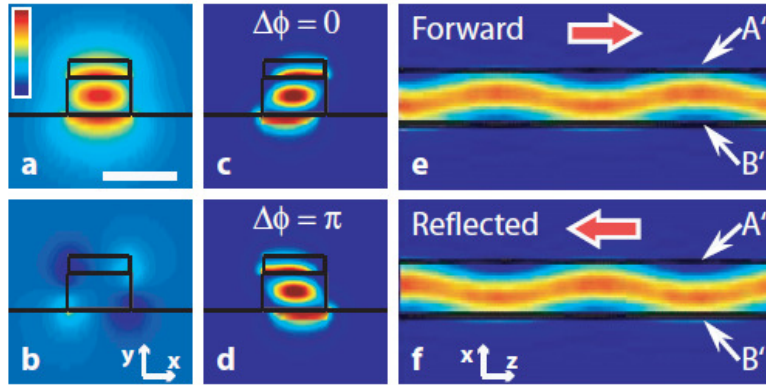


Fig. 3. Interaction between TE and TM modes in high index contrast waveguides. (a) and (b), calculated x - y cross-sectional mode profiles for y component of electric field (E_y) of the TM and TE modes respectively plotted on the same color scale. The 100 nm layer on top of the waveguide represents a thermally grown silicon oxide which acts as a hard mask during reactive ion etching (see Section 6). Note that although the y component of the TE mode (b) is not the major field component, due to the nanoscale waveguide geometry, at the waveguide corners the magnitude of this field is comparable to the magnitude of major component of the TM mode (a). This causes the orthogonally polarized modes to interact. (c) and (d), $|E_y|^2$ for the TM and TE modes summed in-phase and out-of-phase respectively. (e) and (f), x - z cross sections of 3D-FDTD simulations of the evolution of an optical mode consisting of both TE and TM components as it propagates in the forward (+ z) and backward (- z) directions respectively. The forward-propagating and reflected light “lean” toward the points labeled A’ and B’ respectively. These points correspond to A and B in Fig. 2. Scale bar in (a) is 1 μm . All figures are plotted at the same scale. In (a)-(d) the TE mode power has been multiplied by a factor of 4 relative to the TM mode.

Simulations using a 3D Finite Difference Time Domain (FDTD) method verify that forward and backward propagating waves “lean” in opposite directions. Since rectangular high-index-contrast waveguides are typically highly birefringent, the TE and TM modes propagate with different phase velocities due to their different effective indices [31]. The evolving phase difference between the TE and TM modes causes the near-field intensity distribution to oscillate between left and right “leaning” profiles. This can be seen in 3D-FDTD simulations where both the TE and TM modes were launched from left to right (Fig. 3e). Here we plot an x - z cross section through the waveguide 200 nm above the silicon oxide substrate. Note that the waveguides simulated here are free of defects along the waveguide and no reflections are expected. The period of oscillation (L) for this experiment is determined by the birefringence ($\Delta n_{eff}=0.46$ from finite element mode solver) and the wavelength ($\lambda = 1.532 \mu\text{m}$): $L = \lambda / \Delta n_{eff} = 3.3 \mu\text{m}$. This period matches the beat period measured by TRANSOM in Fig. 2a and b. The beating observed here is similar to the polarization mode beating observed in birefringent fibers [16]; however, in low-index-contrast fibers, due to the negligible minor field components, the shape of the mode profile does not change as it propagates. The phase of the oscillation is determined by the initial polarization state (phase relationship between the TE and TM components). The backward-propagating reflected wave is simulated by adding a π phase shift to the TE mode and launching both TE and TM modes from the right of the waveguide (Fig. 3f). As expected, the backward-propagating and forward-propagating light oscillate out of phase with one another, i.e. at each point in the waveguide the modes “lean” in opposite directions. For example, the forward-propagating mode leans toward the point labeled A’ (Fig. 3e) while the backward propagating mode leans away (Fig. 3f). Point B’ shows the opposite behavior. These points correspond to points A and B in Fig. 2. One should note that this behavior does not violate time-reversal symmetry since switching the input and output ends of the waveguide results in identical behavior.

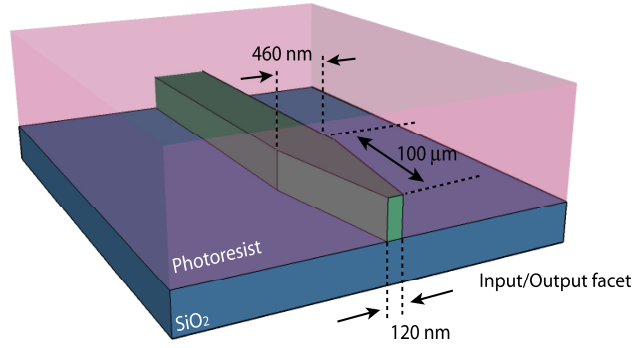


Fig. 4. Schematic of the Si waveguide (green) at the input and output facet. The width of the waveguide is tapered from 460 nm to 120 nm linearly over 100 μm . In this region, the waveguide is clad with S1818 photoresist (approximately 2 μm in height) to prevent the optical mode from leaking into the substrate.

4. Analytical model of near field measurement

The measured data in Fig. 2 matches analytical models which incorporate effects for both forward and backward propagating modes. We can write the change in total power collected (ΔT) at the waveguide output (as a function of probe location x) in terms of the amount of light scattered by the probe:

$$\frac{\Delta T}{T_0}(x) = -\frac{Q}{Z_0} \int_{A(x)} |a_{TM} E_{TM_y} e^{ik_{TM}z} + a_{TE} E_{TE_y} e^{ik_{TE}z}|^2 dA + \eta \frac{Q}{Z_0} \int_{A(x)} |-b_{TM} E_{TM_y} e^{ik_{TM}z} + b_{TE} E_{TE_y} e^{ik_{TE}z}|^2 dA, \quad (1)$$

where ΔT is normalized to the power transmitted in the absence of the probe (T_0). The two terms to the right of the equality represent the scattering of forward-propagating and reflected light respectively (note the sign difference). Also, note the phase (sign) change added to the TE mode in the second term, which is the result of reflection. Here the TM and TE subscripts denote the TE or TM mode respectively and E_y is the y -component of the electric field. The cross-sectional profile of the probe is written as A (see Section 6), x and z are Cartesian coordinates, k is the propagation constant, and Z_0 is the free space impedance.

Due to the large index contrast between the probe and air-cladding, the efficiency with which scattered light couples to the counter-propagating mode (η) is expected to be near unity [13]. For simplicity, we will take this factor to be 1. The amplitudes of the forward and backward propagating modes are written as a and b respectively. We can write b in terms of a according to:

$$b_{TM,TE} = a_{TM,TE} e^{-\alpha_{TM,TE} 2l} R_{TM,TE}, \quad (2)$$

where α is the waveguide loss per unit length, l is the distance between the probe and the source of reflection (the waveguide output in this case) and R is the reflectivity. We take the waveguide loss to be -6.64 dB/cm and -15.36 dB/cm for the TM and TE modes respectively. These values are taken from similar waveguides fabricated in silicon and measured using the cut-back method [32]. The coupling efficiency of each polarization and their respective reflection at the waveguide interfaces is difficult to measure directly; however, the reflection is known to be high, particularly for the TM mode, which despite having lower propagation loss, transmits -11 dB less power through the device as compared to the TE mode. The scattering efficiency (Q) of the probe can be determined by exciting only the TE mode and fitting the TraNSOM data to the convolution of the probe with the y component of the electric field according to [21]:

$$-\frac{\Delta T}{T_0}(x) = \frac{Q}{Z_0} \int_{A(x)} |E_{TEy}|^2 dA \quad (3)$$

Here Q is the sole fitting parameter which we determine to be 25 ± 5 (See Fig. 5).

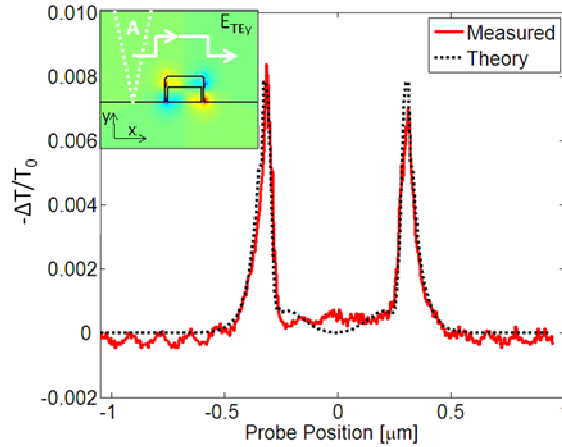


Fig. 5. The measured (solid) and simulated (dotted) TraNSOM trace with a scattering efficiency of $Q = 25$. Inset shows a schematic of the probe cross section A which is convolved over the y component of the TE mode (E_{TEy}) to form the theoretical curve (dotted).

Based on our analytical model (Eqs. (1) and (2)), we identify specific values of reflectivity and ratios of TE to TM excitation which allow forward-propagating and reflected light to be distinguished. Figure 6 shows the maximum change in transmission ($\max[\Delta T/T_0]$) as a function of reflectivity at the chip interface (R) and the relative amplitude of TE mode ($|a_{TE}|^2$). This is calculated from Eqs. (1) and (2), where the probe position (x) is fixed at the location of maximum modal overlap. We keep constant the amplitude of the TM mode ($|a_{TM}|^2=1$, since $\max[\Delta T/T_0]$ depends only the ratio of the modal amplitudes). The reflectivity of the TE mode (R_{TE}) is set to 10% of R_{TM} based on the relative output powers and propagation losses measured above. When scattering by the probe results only in a decrease in power transmitted through the waveguide, $\max[\Delta T/T_0] = 0$ and the forward-propagating and reflected propagating modes cannot be disambiguated. This occurs when the absolute value of the first term in Eq. (1) is always larger than that of the second term. In other words, at each probe position more light is scattered from the forward-propagating light than from the reflected light. We refer to this as the “normal” scattering regime, since as expected, introduction of a scattering point results in a decrease in power transmitted through the waveguide. Conversely, where $\max[\Delta T/T_0] > 0$, forward-propagating and reflected light can be distinguished. In this regime, a scattering point can redirect the backward-propagating reflected light such that the power transmitted through the waveguide increases. Since this is an unexpected consequence of near-field scattering, we refer to this as the “anomalous” scattering regime. The waveguide used for these experiments was designed with $R_{TE} \approx 0.75$ such that the anomalous regime is accessible for ratios of TE to TM excitation > 0.5 which is easily achieved using a polarization controller.

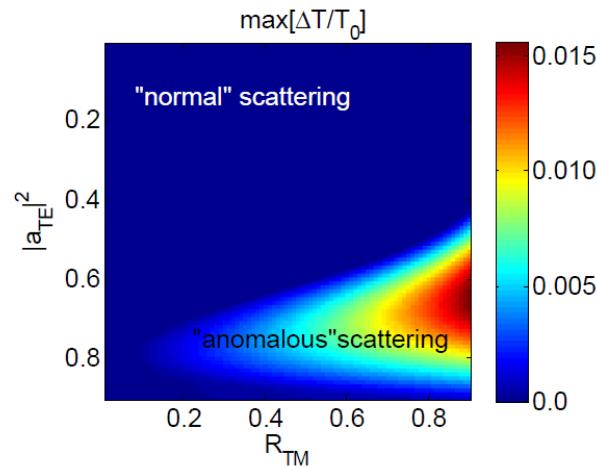


Fig. 6. Change in transmission calculated according to Eq. (1) as a function of relative TE mode amplitude squared ($|a_{TE}|^2$) normalized to total power, and TM reflectivity at the waveguide-fiber interface. The relative reflectivity of the TE mode (R_{TE}) is fixed at $0.1 \cdot R_{TM}$. The “anomalous” scattering regime refers to the region where scattering by the probe results in an increase in the amount of power transmitted through the waveguide. In this region forward-propagating and reflected light can be distinguished by near-field scattering.

We verify our measured results by reproducing the data in Fig. 2a and b using our analytical model. We select from Fig. 6 the point $R_{TM} = 0.75$, and $|a_{TE}|^2 = 0.8$ since this best matches $\max[\Delta T/T_0]$ measured in Fig. 2a. According to Eqs. (1) and (2) we can calculate $\Delta T/T_0$ as a function of x and z . The result plotted in Fig. 2c shows excellent agreement between our model and the measured data shown in Fig. 2a. To confirm that the positive values correspond to backward-propagating reflected light we can remove the second term from Eq. (1) to consider only the forward-propagating mode. Recalculating the image (Fig. 2d) shows that as expected, in the absence of the backward-propagating mode, probe-induced scattering only decreases the power transmitted through the waveguide. This is consistent with our measurement in Fig. 2b, in which we experimentally isolate the effect of only the forward-propagating light. This agreement between our model and the measured data confirms that unlike micron-scale low-index fiber optics, nanoscale waveguides can possess forward and backward traveling waves with unique near-field profiles.

5. Integrated anti-reflection device

Based on the unique mode profiles of forward-propagating and reflected light, novel photonic devices can be developed to selectively attenuate reflected light. Figure 7 shows one potential implementation of such a device that, according to 3D-FDTD simulations, attenuates reflected light by more than -20 dB compared to only -3.6 dB for forward-propagating light. The device is based on a short length of waveguide which can be fabricated near the waveguide input or optical source and has low propagation losses for only one linear combination of TE and TM modes. This particular polarization is used for forward-propagating light. Random defects downstream from this device change the relative amplitude and phase of the TE and TM modes for the reflected light. Therefore, these backward propagating modes experience large propagation losses when they propagate back through the anti-reflection device.

The mode profiles of linear combinations of TE and TM modes (with various phase differences) are shown in Fig. 7 a-c for a square silicon waveguide cladded by silicon dioxide. Since this waveguide is symmetric upon a rotation by 90 degrees, the TE and TM modes are degenerate and propagate with the same phase velocity. Consequently, the phase relationship

between the two fundamental modes remains constant as a function of propagation length (as opposed to the periodic beating seen in the rectangular waveguides discussed above). For example, the left-leaning mode shown in Fig. 7a will remain left-leaning as it propagates along the waveguide (see Fig. 7e). By introducing an absorbing material to a corner of the waveguide (i.e. by doping the Si via ion implantation), attenuation will depend on the phase relationship between the TE and TM modes. If the low-loss mode ($\Delta\phi = 0$) is excited in the forward direction, any random scattering point (not symmetric about the line $y=x$) will reflect light into a higher loss mode by changing the relative amplitude and phase of the TE and TM components.

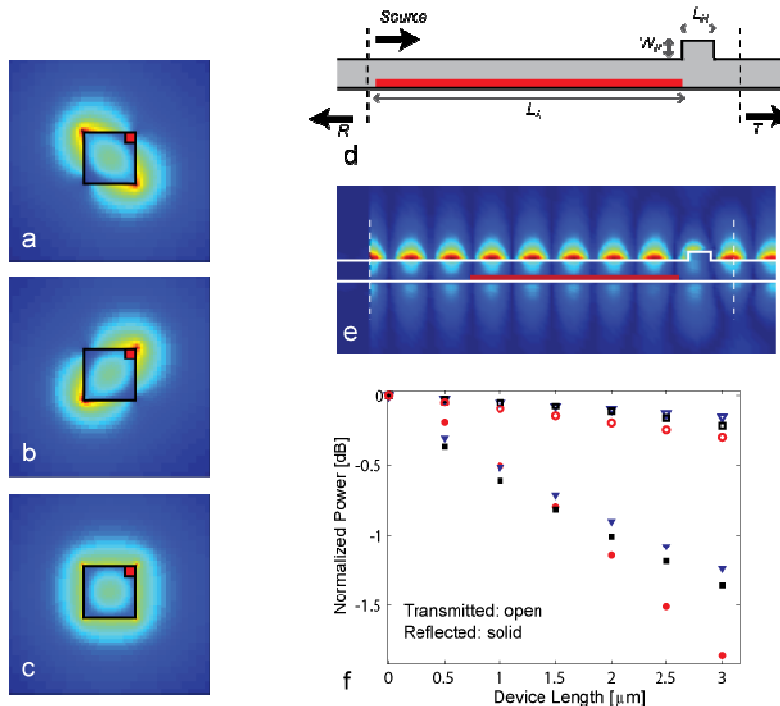


Fig. 7. Simulated performance of anti-reflection waveguide. (a-c) x - y cross-sectional mode profiles showing $|E|$ for various phase differences ($\Delta\phi$) between TE and TM modes (a) 0, (b) π , (c) $\pi/2$. Black counters outline a 250 nm square Si waveguide cladded in SiO₂. The red box indicates a 50 x 50 nm region of optically absorbing material (i.e. doped Si). Based on the mode overlap with the lossy region, propagation losses for the modes are calculated to be: (a) 0.13 dB/ μ m, (b) 0.77 dB/ μ m, (c) 0.45 dB/ μ m. (d) x - z cross-sectional schematic of the 3DFDTD simulations of the proposed device. The low loss mode ($\Delta\phi = 0$) is launched from left to right and propagates over a length of waveguide (L_A) with an absorbing corner. A scattering point is represented as an increased waveguide with (W_R) over a length (L_R). This defect reflects light back toward the source. Reflected and transmitted power is monitored at the planes indicated by the dashed lines. An x - y cross section of waveguide in the absorbing region is shown in (a) where the red box indicates the location of highly doped Si. (e) snapshot of the x -component of the electric field taken through a plane 50 nm from the top of the waveguide showing the forward propagating mode leans away from the absorbing region. (f) Normalized Power Transmitted (open symbols) and Reflected (solid symbols) as a function of device length for various configurations of the scattering point: triangles: L_R :0.05, W_R :0.01, squares: 0.10, 0.20 circles: 0.30, 0.10 (all dimensions in μ m).

Figure 7d shows a schematic of a proposed anti-reflection device to be placed near the waveguide input or on-chip optical source. This region is most sensitive to reflection since optical intensity is highest near the input. The device consists of a short length of square waveguide with an absorbing region at the waveguide corner. In this case, we design the top

right corner of the waveguide (50x50 nm) to be highly doped, yielding an imaginary part of the permittivity equal to 9.3 for a length L_A . As a generalized point of reflection, the waveguide is made wider by a width of W_R and a length L_R as shown in Fig. 7d. This defect is placed downstream of the proposed device as this represents the most probable configuration. Since the device footprint is on the order of 10 μm and optical path lengths in typical photonic circuits stretch for distances on the order of 1 cm, more than 99% of the waveguide defects will occur in the region downstream of the device (assuming a uniform defect probability density). These defects could also include impedance mismatches at photonic elements such as ring resonators placed next to waveguides, or transitions from one waveguide to another. The distance between the device and defect does not affect the relative attenuation of forward and backward propagating modes. To simulate device performance, forward-propagating light is excited as a linear combination of in-phase TE and TM modes of equal amplitude, 4 μm away from the point of reflection traveling from left to right. Power monitors to the right of point of reflection and to the left of the source record the amplitude of the transmitted and reflected power respectively. Integrated polarization rotators [18, 19] could be used to prepare the appropriate linear combination of TE and TM modes and convert the transmitted light to other polarizations if desired.

Based on 3D-FDTD simulations the proposed device exhibits higher propagation losses for reflected light compared to forward-propagating light. The amplitude of the transmitted and reflected power as a function of L_A for various configurations of the reflection point is plotted as the open and solid symbols in Fig. 7e respectively. To compare the relative attenuation of the reflected and transmitted power, the amplitude of each is normalized to 1 for $L_A = 0$. The length and width (in microns) of the reflecting point was chosen at random to be: 0.05, 0.10 (triangles) 0.1, 0.2 (squares) 0.3, 0.1 (circles) respectively. As shown in Fig. 7e, for all three configurations, increasing the length of the absorbing region attenuates the reflected light at a greater rate compared to the transmitted light. The propagation loss for the forward propagating modes is approximately -0.08 ± 0.02 dB/ μm along the device length, while the propagation losses for the reflected light varied from 0.36 to 0.67 dB/ μm . These values compare favorably with the propagation losses calculated from the mode overlaps in Fig. 7a-c. For the phase differences of 0, $\pi/2$, and π (shown in Fig. 7 a-c respectively), the corresponding propagation losses are approximately -0.13 , -0.45 , and -0.77 dB/ μm assuming a p-type doping concentration of $2 \times 10^{17}/\text{cm}^3$ and a corresponding imaginary part of the permittivity of 9.3 [33]. Since the losses are exponential as a function of device length, the extinction ratio can be increased by increasing the length of the absorbing region. Based on the propagation losses in Fig. 7f, extending L_A to 45 μm will reduce the power reflected by all three of the defects by an average of -21 dB while attenuating the transmitted power by only -3.6 dB. Compared to previously reported magnet-optic-based photonic isolators, this device would have a much smaller footprint while maintaining similar extinction ratios [34, 35]. While this device is only a representative geometry which could likely be optimized, the calculated extinction ratio over a 45 μm long region could provide a practical method to attenuate light reflected at waveguide interfaces, photonic devices, or areas prone to waveguide defects.

6. Methods

Silicon-on-insulator (SOI) waveguides are approximately 1 cm long, 460 nm wide, and 260 nm tall covered with a 130 nm tall thermally-grown oxide which served as a hard mask during reactive ion etching. No reflecting defects have been intentionally added to the waveguides during fabrication. SOI substrates purchased from Soitec have a 3 μm thick buried oxide layer. The fabrication method is similar to that described in [21].

For calculations of the mode overlap with the scanning probe, the cross-sectional profile of the near-field probe, A , was modeled as an inverted triangle with a half angle of 10° (Manufacturer's specifications, Nanosensors). At each position (x) the y coordinate of the

profile is chosen such that the probe is positioned in contact with the surface (see Fig. 5). Finite difference mode solvers and 3D-FDTD code was developed by Christina Manolatu. Analysis and figures were generated using Matlab.

The optical source used for the experiments is a multi-line external cavity laser (ECL) amplified with a 120 mW EDFA (JDS Uniphase) and filtered using a 1.4 nm FWHM tunable bandpass filter (TBF) centered at 1532 nm. The linewidth of the external cavity laser was less than the resolution of our optical spectrum analyzer (<10 pm). The output of the TBF was sent through a digital polarization controller (HP) which we used to polarize the input to excite a combination of TE and TM modes. For the short-coherence-length measurements the ECL was turned off leaving 1.4 nm bandwidth amplified spontaneous emission as our source. Light was coupled into and out of the waveguide using fibers glued to the waveguide facets using a UV curable epoxy (see [21] for details of the packaging). In all cases, a single optical source is used to illuminate the waveguide from only the input side. The waveguide was imaged with a Dimension 3100 atomic force microscope using a Pt/Ir coated AFM probe from Nanosensors. The waveguide output was collected into a fiber glued to the waveguide facet and measured with a Newport 1818-IG photodetector and 2832c power meter. The analog output of the power meter was amplified using an HP voltage pre-amplifier with a 30 Hz low pass filter and then sent to the analog input of the AFM for simultaneous recording with the waveguide topography.

7. Conclusion

The distinct near-field profiles for counter-propagating waves reveal fundamental differences between optical propagation in nanoscale waveguides compared to free-space and fiber optics. This phenomenon is solely a consequence of strong optical confinement and is likely to occur in the nanoscale high-index waveguides that are used widely in industrial and academic research labs. In addition to potentially affecting device performance, this phenomenon could be utilized as a basis for selectively attenuating reflected waves. Active components or specific waveguide geometries could be developed to create uni-directional integrated devices which could limit the intensity of reflected light. This would provide a path toward developing robust nanophotonic devices and architectures unhindered by optical reflections.

Acknowledgments

The authors thank A. Falk, F. Koppens, and N. de Leon for their comments on the manuscript. Research support is gratefully acknowledged from the National Science Foundation's CAREER Grant No. 0446571. This work was performed in part at the Cornell NanoScale Facility, a member of the National Nanotechnology Infrastructure Network, which is supported by the National Science Foundation (Grant ECS 03-35765) and we made use of STC shared experimental facilities supported by the National Science Foundation under Agreement No. ECS-9876771.